

<https://doi.org/10.1038/s41528-024-00328-w>

Transient shuttle for a widespread neural probe with minimal perturbation



Yeonwook Roh^{1,4}, Hyeongseok Kim^{1,4}, Eun-A Kim^{2,4}, Kyungbin Ji^{1,4}, Minji Kang¹, Dohyeon Gong¹, Sunghoon Im¹, Insic Hong¹, Jieun Park¹, Soo Jung Park², Yiseul Bae², Jae-Il Park³, Je-Sung Koh¹, Seungyong Han¹, Eun Jeong Lee²✉ & Daeshik Kang¹✉

Bioelectronic implants in the deep brain provide the opportunity to monitor deep brain activity with potential applications in disease diagnostics and treatment. However, mechanical mismatch between a probe and brain tissue can cause surgical trauma in the brain and limit chronic probe-based monitoring, leading to performance degradation. Here, we report a transient shuttle-based probe consisting of a PVA and a mesh-type probe. A rigid shuttle based on PVA implants an ultrathin mesh probe in the target deep brain without a tangle, while creating both a sharp edge for facile penetration into the brain and an anti-friction layer between the probe and brain tissue through dissolving its surface. The capability to shuttle dissolved materials can exclude the retracted process of the shuttle in the brain. Complete dissolution of the shuttle provides a dramatic decrease (~ 1078 -fold) in the stiffness of the probe, which can therefore chronically monitor a wide area of the brain. These results indicate the ability to use a simplistic design for implantation of wide and deep brain probes while preventing unnecessary damage to the brain and probe degradation during long-term use.

Long-term monitoring of deep brain activity across a wide range of regions could reveal underlying mechanisms of disease and recognition^{1–6}. A typical approach for determining the exact location of electrodes for monitoring deep in the brain is surface penetration with high rigidity probes^{7–12}. However, achieving such a facile implant of probe into the soft brain through rigidity is a critical challenge for chronic monitoring of the brain. The high stiffness mismatch between the rigid probe and soft brain tissue induces gliosis in the probe as an immune response, as indicated by long-term measurements of the probe^{13–17}. Additionally, movement of the brain implanted with a rigid probe may disturb the stability of the recording of the probe^{14,18–20}.

A flexible probe constructed from materials and structures is a remarkable strategy for accessing chronic implants in the deep brain^{21–25}. A flexible probe with a stiffness that is relatively similar to that of soft brain tissue does not cause degradation of the recording of the probe or functional recovery of the wounded neurons. Such a probe requires rigid shuttle-assisted implantation to be transferred to the inner brain, which is difficult to penetrate. However, the rigidity of the shuttle can cause the mechanical mismatching between the soft brain and the rigid shuttle, potentially leading to scratches. Additionally, withdrawal of the shuttle after transfer of the probe causes further injury, which is again associated with friction and pulls

the brain in the direction of withdrawal^{26–28}. In particular, implantation in a wide area of the brain can increase the possibility of secondary damage. Approach of using soluble materials as a supporting layer to prevent the bending can be leveraged for implanting the flexible electronics into the deep brain^{29–31}. However, these implants are restricted to relatively narrow areas of the brain or require the withdrawal of the shuttle due to the long soluble time, leading to the secondary shear stress on the tissues. Additionally, the process of withdrawing the shuttle may cause bending or extraction of the implanted electronics due to adhesion between melted shuttle and the implanted probe.

Here, we report the use of a transient shuttle-based probe to minimize secondary damage during wide and deep brain implantation. The changeable stiffness (1078-fold) of this system obtained by means of dissolvable PVA enables the ultrathin mesh electrode (thickness: 10 μm) to penetrate the brain through high bending stiffness (3.59 nN m^2) without tangles and to be implanted in the deep brain in a state of low bending stiffness (3.33 pN m^2). Dissolvability of the PVA results in the formation of a sharp edge and lubricant layer, decreasing the damage resulting from penetration and shear stress between the probe and the target brain tissue during insertion, respectively. After insertion of the probe system, the fully dissolved shuttle of the PVA does not require the withdrawal of the shuttle,

¹Multiscale Bioinspired Technology Lab, Department of Mechanical Engineering, Ajou University, Suwon-si, Gyeonggi-do, Republic of Korea. ²Molecular Neurocircuits Lab, Department of Brain Science, Ajou University School of Medicine, Suwon-si, Gyeonggi-do, Republic of Korea. ³Gwangju Center, Korea Basic Science Institute (KBSI), Gwangju, Republic of Korea. ⁴These authors contributed equally: Yeonwook Roh, Hyeongseok Kim, Eun-A Kim, Kyungbin Ji.

✉ e-mail: elee@ajou.ac.kr; dskang@ajou.ac.kr

preventing the damage and displacement of the probe from the target position with the tangle. Additionally, the flexibility of the mesh electrode achieved through dissolving the shuttle is suitable for chronic implantation, exhibiting a minimal immune response in the mouse brain. Moreover, during such testing, neurons gradually approach the mesh electrode during implantation due to the small gap in stiffness between the probe and brain.

Results

Overview of transient shuttle-based probe for implantation into the brain

A schematic illustration, as shown in Fig. 1a, shows the onboard mesh electrode in the transient shuttle based on the PVA for insertion into the brain. Due to the relatively high stiffness of the PVA, flexible mesh-type electrodes were embedded for insertion into the brain without bending (Fig. 1b). Additionally, dissolution of PVA in the brain provides flexibility to the mesh electrode in the implanted state to prevent chronic inflammatory reactions. This change in stiffness of the transient shuttle-based probe originates from the reaction with moisture (Fig. 1c)³². Here, cutting of agarose gel through PVA summarize an ability of rigidity change in the transient shuttle (Supplementary Fig. 1). PVA is readily dissolvable in a moisture-rich agarose gel after cutting. This dissolvable transient shuttle simultaneously offers rigidity for insertion and flexibility for chronic implantation of the mesh electrode, achieved through a stiffness change (before insertion: 3.59 nN m^2 , after insertion: 3.33 pN m^2) of ~ 1078 -fold (Fig. 1d and Supplementary Fig. 2). Another advantage of the transient shuttling of PVA is creating the sharp edge and lubrication layer of inserting probes. A dissolvable PVA coating decreases the stress between the probe and the brain tissue and the associated damage from the penetration and scratches to the tissue (Fig. 1e).

Figure 1f shows sequential images of the transient shuttle-based probe implanted in the agarose gel phantom. A mesh electrode connected to an inserter through a PVA coating of high stiffness penetrates the agarose gel and occupies the desired position without a tangle. Furthermore, the process of withdrawing the inserter after dissolving the PVA shuttle does not influence the position of the implanted mesh electrode without dragging into the inserter. This approach using stiffness changes of the transient shuttle-based probe, as shown by immunostaining in Fig. 1g, h, demonstrated chronic implantation of the mesh electrode in a widespread area of the deep brain of mice. Injury to brain tissue accompanies surgical damage to neurons and an acute inflammatory response in the initial state, but these phenomena are not connected to a decrease in neuron density or a chronic inflammatory response over time (~ 6 weeks) (Fig. 1i). Additional details on the rigidity decreases of the transient shuttle-based probe appear in Supplementary Note 1 and Supplementary Fig. 2.

Mechanical characteristics of transient shuttle-based probes during insertion

The stable insertion of a neural probe into targeted brain tissue requires high stiffness for penetration without bending or buckling³³. Figure 2a shows the fabrication process of the transient shuttle-based probe (width: 2.14 mm, height: 4 mm, thickness: $60 \mu\text{m}$) consisting of PVA and a mesh-type electrode (thickness of SU-8: $10 \mu\text{m}$). The process was as follows: a PVA solution was poured into a mesh electrode and inserted into a PDMS mold. The mesh electrode encapsulated with the PVA solution was oven cured for 30 min and then separated from the PDMS mold. The details of the fabrication process, including the mesh electrode, are provided in the Supplementary Methods and Supplementary Fig. 3. Figure 2b and Supplementary Fig. 4 present sequential images of the transient shuttle-based probe soaked in PBS ($\sim 37^\circ\text{C}$). The diffusion of water into the voids of the mesh electrode enables the prompt dissolution and separation of the mesh electrode with the inserter (~ 6 min) (Fig. 2c and Supplementary Fig. 5). Supplementary Video 1 summarizes the process of separating the mesh electrode through dissolving the transient shuttle of PVA.

To test the insertion of the transient shuttle-based probe into the target point without incurring mechanical failure, we fabricated the brain tissue

phantom using agarose gel (0.6 wt%, shear modulus: 615 Pa), similar to the rigidity of the brain (Supplementary Fig. 6)^{34,35}. Figure 2d shows the process of inserting the probe into the agarose gel after soaking in liquid nitrogen to delay the decrease in rigidity of PVA. When inserting the probe into gel, dissolving of PVA starting from the contact edge with gel changed the footprint of the shuttle with the sharp shape. Due to this decrease of the footprint, the probe was able to cross the agarose gel without bending and was located at the target position in the widespread state (Fig. 2e). The PVA coating of the probe also influenced the minimized friction with the targeted tissue as well as facile penetration. Supplementary Fig. 7a, b present coated materials can minimize the friction and associated scratches to the tissue. To decouple effect of the stress reduction via the decrease of the footprint, we design test using SU-8 and oiled SU-8, where SU-8 does not dissolve in the agarose gel to exclude the effect of the footprint decrease. Insertion of the SU-8 and oiled SU-8 into agarose gel yielded the similar normal stress (first peak) during the penetration of agarose gel's surface, respectively. After penetrating the agarose gel's surface, both sides of SU-8 contacts with the gel, which induces the shear stress (second peak) between the SU-8 and the agarose gel. In contrast to the relative high shear stress observed during the surface penetration of SU-8 without oil, oiled SU-8 was able to reduce the shear stress. The phenomenon becomes more apparent when the frictional force of PVA-coated probe and noncoated probe is measured and compared on a wet surface (Fig. 2f). The anti-friction layer through dissolved PVA yields a relatively low frictional force. Another factor that influences the stress to the brain is the insertion speed of the PVA-coated probe. To determine the optimum insertion speed, we inserted the probe at a range of different speeds (1 mm s^{-1} , $500 \mu\text{m s}^{-1}$, $250 \mu\text{m s}^{-1}$, and $100 \mu\text{m s}^{-1}$). When inserting the probe at $500 \mu\text{m s}^{-1}$, the measured force is relatively low, compared to that at 1 mm s^{-1} (Supplementary Fig. 8a, b). However, the slower speeds of insertion ($250 \mu\text{m s}^{-1}$ and $100 \mu\text{m s}^{-1}$) resulted in the bending of the transient shuttle due to dissolution (Supplementary Fig. 8c, d). This reduction in footprint and friction decreased both the normal and shear stress between the probe and the agarose gel at the optimum insertion speed ($500 \mu\text{m s}^{-1}$) (Fig. 2g). Additionally, the FEA simulation results with and without the PVA coating, as shown in Fig. 2h, i, demonstrate that, compared with the uncoated probe, the transient shuttle-based probe easily penetrates the target tissue with low friction. This facile fabrication of the transient shuttle potentially enables the various designs of mesh electrodes to be dependent on the monitored tissue of the brain (Supplementary Fig. 9). Similarly, the transient shuttle of PVA transfers mesh electrodes of complex design into agarose gels without tangles (Fig. 2j).

Mechanical characteristics of transient shuttle-based probes during withdrawal

An external force for withdrawing a shuttle may cause the mesh electrode to be implanted in an undesirable position while the mesh is angled. Additionally, pulling accompanied by friction between the shuttle and the brain can yield secondary damage^{26,36}. To validate that the transient shuttle prevents this secondary damage, we compared the forces applied to the agarose gel during inserter withdrawal between transient and non-transient shuttles. Fully dissolving PVA in the connecting site, as shown in Fig. 3a, did not cause an entangled mesh electrode in the agarose gel during the withdrawal of the inserter. Achieving such a withdrawal, without influencing the position of the mesh electrode, has the advantage of preventing secondary damage in the brain. For example, a transient shuttle that can disconnect a mesh electrode, as shown in Fig. 3b, exhibits minimal frictional force in the inserted area of the mesh electrode. Conversely, the non-transient shuttle induces frictional force during withdrawal (Fig. 3c). Additionally, retraction process of the non-transient shuttle may risk entangling the flexible mesh electrode (Supplementary Fig. 10). Supplementary Video 2 depicts insertion of the probe and withdrawal of the inserter into and out of the agarose gel.

Because mechanical mismatching between the probe and brain increases the possibility of an inflammatory immune response in the brain and disturbs stable monitoring during movement, flexibility accompanied by low bending stiffness is crucial for implantation for a long period^{37–39}.

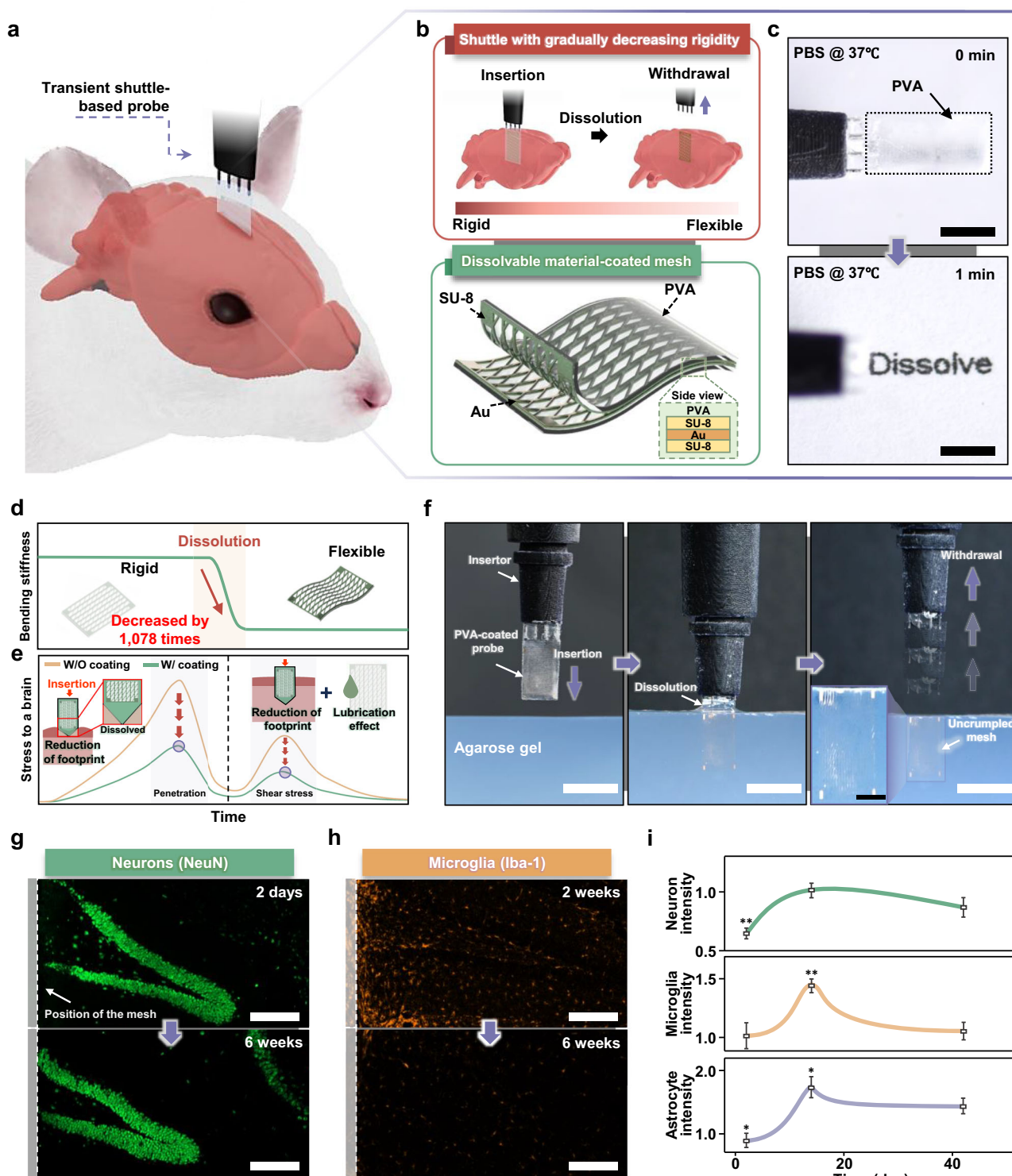


Fig. 1 | Transient shuttle-based probe for chronic implant without secondary damage into a brain. **a** Schematic illustration of the transient shuttle-based probe inserted into the mouse brain. **b** Changes in the rigidity of the transient shuttle-based probe (PVA-coated mesh electrode) during the implantation process. **c** Sequential images for dissolving PVA in a PBS solution at 37 °C (scale bar: 2 mm). **d**, **e** Schematic illustration and graph of the (d) stiffness change (before insertion: 3.59 nN m², after insertion: 3.33 pN m²) and (e) stress minimization to the brain through the decrease of the contact area and lubrication effect for inserting the transient shuttle-based probe. **f** Sequential image of the process of implanting the

probe into the agarose gel (scale bar: 3 mm, 1 mm (inset)). **g**, **h** Confocal fluorescence microscopy images of (g) neuronal and (h) microglial changes in brain tissue during implantation of the probe (scale bar: 200 μm). **i** Experimental intensity data for neurons and microglia within 0–25 mm proximity to the probe were recorded at intervals of 2 days, 2 weeks, and 6 weeks post-implantation (repeated on *N* = 3 independent samples; all error bars represent mean ± s.e.m.; independent two-sample *t* test), and trend graphs were constructed based on the outcomes of the statistical significance tests. **P* < 0.05, ***P* < 0.01 (Student's *t* test). Panels **a** and **b** are reproduced with permission from Turbosquid and 3D models.

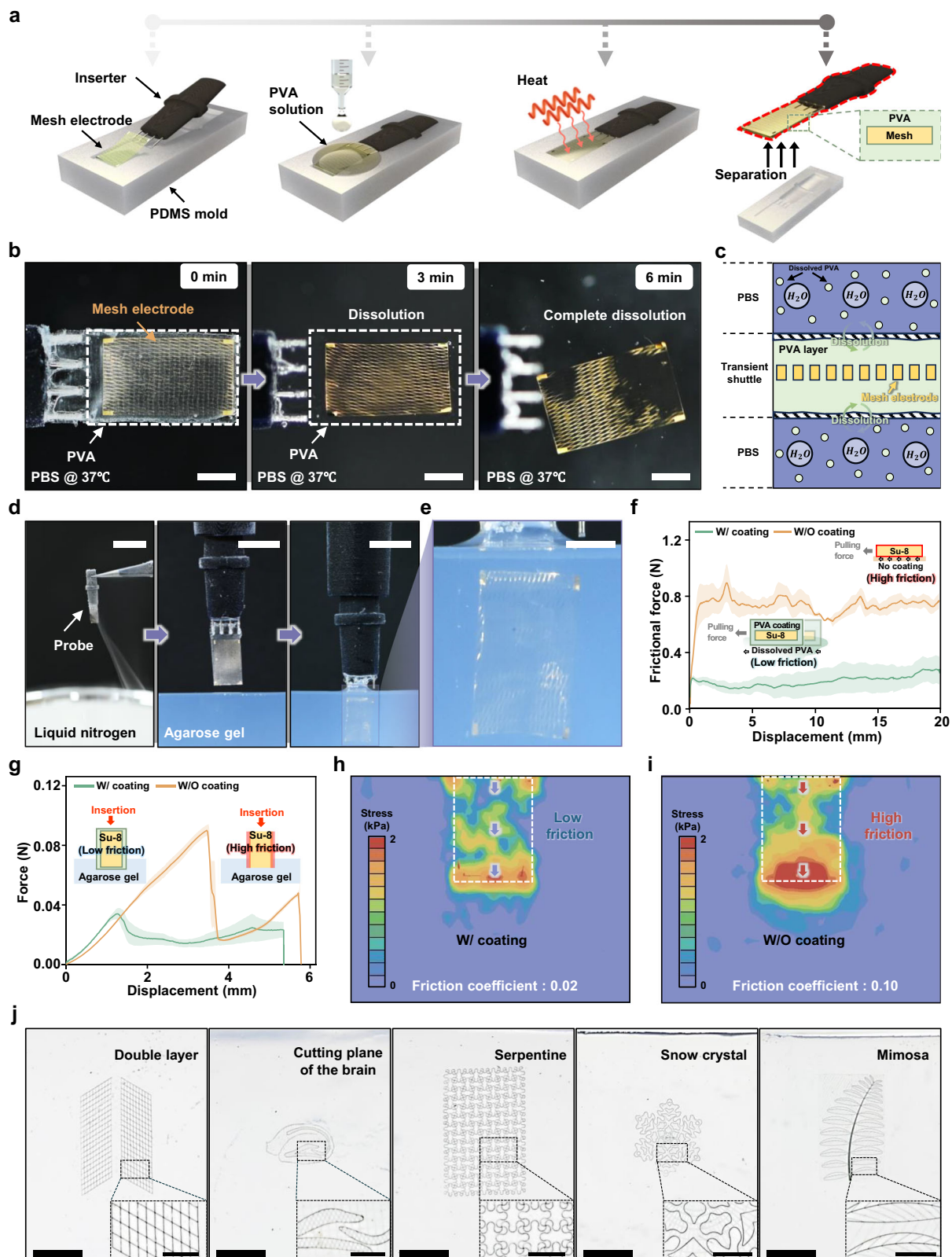


Fig. 2 | Characterization of the transient shuttle-based probe for insertion.

a Fabrication process for the transient shuttle-based probe using PVA and a mesh electrode. **b** Sequential images for dissolving the mesh electrode embedded in PVA in PBS solution. **c** Schematic image of the separation process of the mesh electrode from PVA in PBS solution (scale bar: 1 mm). **d** Sequential images of the process of inserting the transient shuttle-based probe into an agarose gel (scale bar: 1 cm (left), 3 mm (middle), 3 mm (right)). **e** Photograph image of a widespread probe in an

agarose gel without a tangle (scale bar: 1 mm). **f** Comparison of the friction properties of the probe with and without the PVA coating in a wet environment ($N = 3$: N is the number of the repeated measurements). **g** Comparison of the shear forces of the probe with and without the PVA coating during insertion ($N = 3$). **h**, **i** FEA models of the inserted probe with and without the PVA coating. **j** Photographic images of various designs of inserted mesh electrodes through a transient shuttle in an agarose gel (scale bar: 2 mm, 500 μ m (inset)).

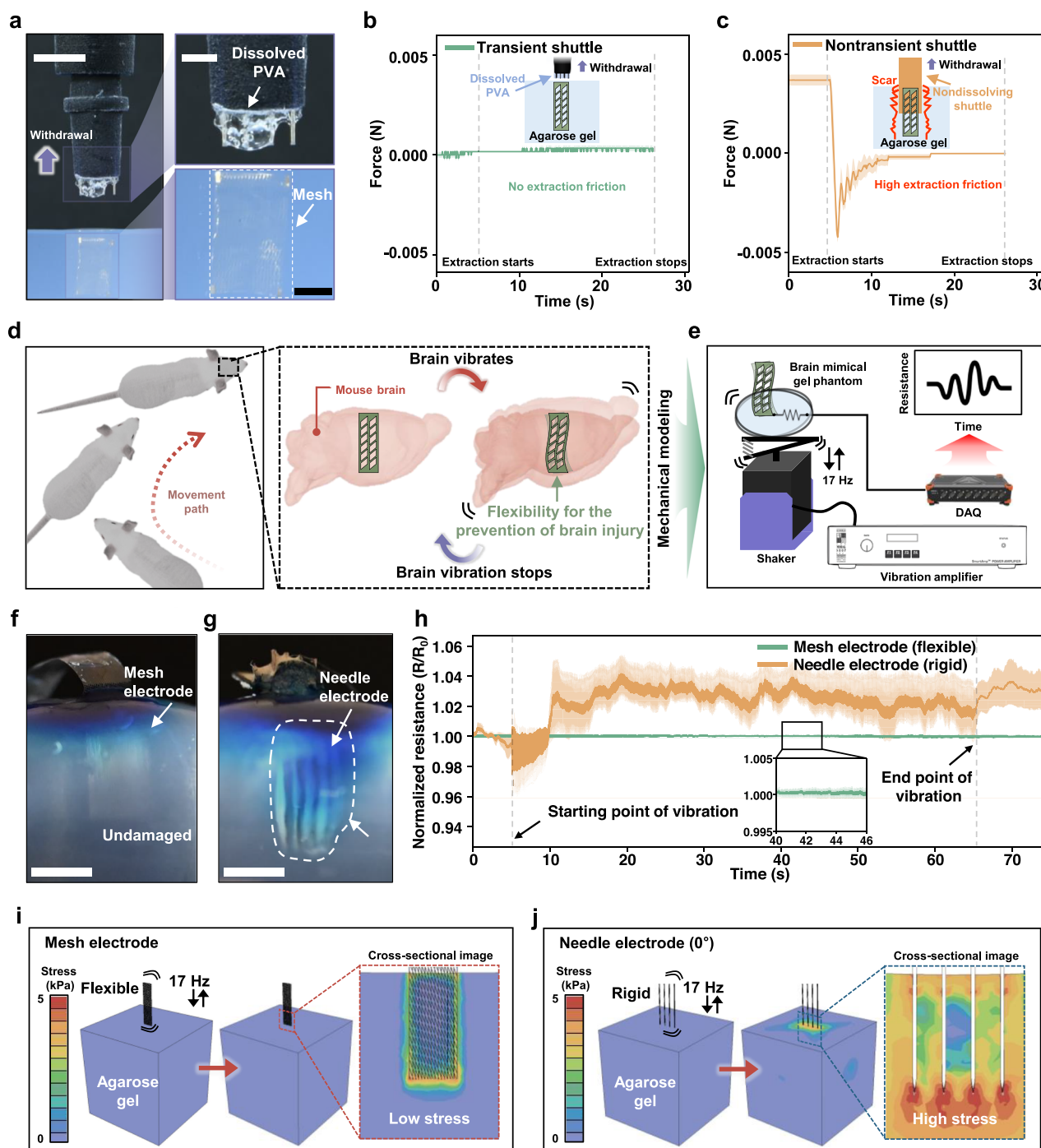


Fig. 3 | Mechanical characterization of the transient shuttle-based probe for a withdrawal and chronic implant. **a** Photograph image of a mesh electrode disconnected from the inserter (scale bar: 3 mm (left), 1 mm (right)). **b**, **c** Force measured during withdrawal of the inserter connected with (b) the transient and (c) nontransient shuttle ($N = 3$; N is the number of the repeated measurements). **d** Schematic illustration of the behavior of an implanted mesh electrode in a swayed brain. **e** Schematic illustration of the mechanical modeling used to confirm the

performance of the mesh electrode in the dynamic state. **f** Unbroken agarose gel with the mesh electrode for the vibration test (scale bar: 2 mm). **g** Broken agarose gel with a needle electrode for a vibration test (scale bar: 2 mm). **h** Comparison of the resistance changes in the mesh and needle electrode for the vibration test ($N = 3$). **i**, **j** FEA models of the implanted mesh and needle electrode in the swayed state. Panel d is reproduced with permission from Turbosquid and 3D models.

Figure 3d shows the behavior of a mouse implanting the mesh electrode through the transient shuttle, where the mesh electrode can follow brain movement without disconnection or damage to the brain. To test the mechanical stability of the inserted mesh electrode in the brain, we designed the test using a vibration shaker incorporating the spring dampers that simulates the movement of the user-implanting mesh electrode (Fig. 3e,

Supplementary Video 3, and Supplementary Fig. 11). The mesh and rigid electrode are fixed at a rigid shell after insertion into agarose gel. A fast, dissolvable transient shuttle (~6 min) in a wet environment can provide stiffness matching that of the mesh electrode and brain tissue after effective insertion using high bending stiffness. In this case, the vibration into the mesh electrode did not disrupt the agarose gel because of an ~1078-fold

decrease in stiffness after its insertion (Fig. 3f and Supplementary Fig. 12a). In contrast, when the rigid probe was used to separate the agarose gel, the blue dye permeated the gel (Fig. 3g and Supplementary Fig. 12b). Such mechanical mismatching disturbs the stable measurement of electrical signals from nerve cells. Figure 3h shows a comparison of the electrical resistance changes in the mesh and needle electrodes for the vibrated situation (~ 17 Hz). After the electrode was removed from the PVA coating, the electrical resistance was stably monitored through flexibility following the shaking procedure (Supplementary Fig. 13). The rigid needle electrode causes unstable electrical signals resulting from connection and disconnection with the split agarose gel. The results of finite element analysis (FEA) of the mesh and needle electrodes, as shown in Fig. 3i, j, highlight the possibility of chronic implantation of the mesh electrode being transferred by the transient shuttle in the brain. The vibration applied to the needle electrode in an agarose gel generates a distribution of relatively high stress outside the implanted area of the electrode compared to that of the area covered by the mesh electrode.

In vivo test using mouse brains for insertion and withdrawal

Figure 4a and Supplementary Video 4 show the results of an in vivo test in which a mouse was used to confirm the ability of the transient shuttle-based probe to prevent secondary damage during insertion of the mesh electrode and withdrawal of the inserter. The designed experimental set, as shown in Supplementary Fig. 14, allows the implantation of the transient shuttle-based probe at a constant speed (~ 1 mm s $^{-1}$). To validate the ability of the transient shuttle-based probe to prevent secondary damage, the insertion test involves the insertion and withdrawal of the transient shuttle and a reference non-transient shuttle (Fig. 4b). When the transient shuttle was inserted, the relatively low friction and shear forces (~ 43.5 mN) effectively decreased the damage in the brain through the lubrication effect and the reduced footprint of the dissolved PVA. In contrast, non-transient shuttling based on the SU-8 intensely scrapes the brain, resulting from high friction and shear force (~ 76 mN) between the brain and the shuttle. Such shear stress in the brain gradually decreases but may cause surgical damage (~ 10 mN) until withdrawal of the shuttle¹⁵. Moreover, attachment of brain tissue to a non-transient shuttle after its insertion induces a pulling force (~ 27.5 mN) and associated damage to the brain when the shuttle is withdrawn¹³. Conversely, the transient shuttle becomes fully dissolved in the brain without the potential scratch to the tissue, eliminating the withdrawal process of the shuttle. When the probe implantation was complete, the measured pulse wave in the mouse brain indicated the survival of the mouse during and after the probe implantation (Supplementary Fig. 15).

Figure 4c shows the position of the mesh electrode transferred by the transient shuttle into the mouse brain (width: 9.5 mm, length: 15 mm, depth: 6 mm), from which the inserter was withdrawn. The mesh electrode (width: 2.14 mm, length: 4 mm) was inserted to a depth of 4.5 mm at positions approximately +1.5 to +2.0 mm ML (medial-lateral) from the midline of the mouse brain. As shown in Fig. 4d, we intentionally embedded the electrode in the vertical direction in the mesh to provide intuitive insight into the straightened or tangle state of the electrode in the micro-CT image. Due to the transient shuttling of high bending stiffness, the mesh electrode could be straightened into the targeted mouse brain without requiring a tangle (Fig. 4e and Supplementary Fig. 16). Figure 4f shows the horizontally measured fluorescence intensity, which indicates the gap between the lines of the mesh electrode at regular intervals spanning the depth of the brain (0.5–3.0 mm). Here, the inserted metal electrode spacing (~ 130 μ m) at most measured points is similar to the initial gap between electrodes (130 μ m) before insertion (Fig. 4g). Effectively delivering the mesh electrode through the transient shuttle became more pronounced while maintaining the constant vertical length of the electrode of the mesh after insertion (Fig. 4h). A relatively minor change in the vertical length of the metal line ($\sim 2\%$), as well as its equal line spacing, demonstrated that the transient shuttle can be used to implant the mesh electrode without a tangle in the mouse brain. The detailed process of measuring the electrode gap and length is provided in Supplementary Note 2.

Histology studies of chronic implantation of the transient shuttle-based probe in mouse brains

Stiffness mismatching between a probe and brain tissue for chronic implantation causes a foreign body reaction (e.g., microglia and astrocytes) and associated degradation of the probe performance^{40–42}. Chronic inflammatory cells in the scarred tissue at the inserted position also disturb the regeneration of neurons⁴³. Figure 5 shows the results of histological studies of mouse brains chronically implanted with mesh electrodes transferred by the transient shuttle. The brain tissue was stained with neuronal nuclear antigen (NeuN, green) to label neurons, ionized calcium-binding adapter molecule (IBA1, orange) to label microglia or glial fibrillary acidic protein (GFAP, orange) to label astrocytes together with 4',6-diamidino-2-phenylindole (DAPI, Blue) to label all nuclei. The mouse brain was sliced with a mesh electrode to evaluate changes in the behavior of neurons and the immune response over the course of the experiment. The detailed process of staining the mouse brain sections is provided in Supplementary Note 3.

Figure 5a, b shows the behavior of neurons and microglia or astrocytes of the dentate gyrus (Fig. 5c) near the implantation position of the transient shuttle-based probe for 6 weeks. The white dashed line indicates the boundary of the mesh electrode implanted into the brain. Insertion of a rigid transient shuttle damages tissue near the probe (distance from the probe: ~ 130 μ m), including neurons, in the initial period. However, promptly dissolving shuttles in the brain increases the flexibility of the mesh electrode for the regeneration of neurons adjacent to the implanted position between 2 and 6 weeks after insertion (distance from the probe: ~ 60 μ m) (Fig. 5d). In contrast, SU-8 film promotes neuronal regeneration starting only 6 weeks after insertion (Supplementary Fig. 17a). The intensity of neurons and glia cells like microglia and astrocytes near the mesh electrode is an important indicator for confirming the possibility of chronic implantation of a transient shuttle-based probe and monitoring neural signals. An intensity measurement method of the neurons, microglia and astrocytes according to each period is explained in Supplementary Note 4 and Supplementary Fig. 18. To briefly explain the process for this test, we grouped the image pixels into groups with 25 μ m intervals to comparatively analyze the brain tissue at risk of being influenced (distance from the probe: 0–400 μ m) and the noninfluenced brain tissue (distance from the probe: 400–425 μ m) for surgical damage. Figure 5e–g shows the changes in the intensities of neurons, microglia and astrocytes at 2 days, 2 weeks, and 6 weeks, respectively. Although the neuron intensity, calculated as the distance from the mesh electrode surface across the entire range, was relatively uneven during the initial period of implantation, an increase in the neuron intensity near the mesh electrode demonstrated the stability of the mesh electrode in the brain, in addition to the former resulting in a decrease in the distance between the mesh electrode and neurons (Fig. 5e). The phenomenon of stable movement of the chronically implanted mesh electrode became more pronounced when the number of microglia that responded to the foreign object decreased over time, as shown in Fig. 5f. For an initial period of 2 weeks, the presence of the mesh electrode in the tissue elicits relatively high numbers of microglia, which is attributable to the acute immune response. However, such an acute immune response does not progress with a chronic inflammatory response through dissolution of the rigid coating of the mesh electrode, which was proven by immunostaining for microglia at 6 weeks after the insertion of the probes. Activation of astrocytes, another marker of neuroinflammation, was observed in the brain regions near the mesh probe 2 weeks after insertion, but this activation had subsided by 6 weeks after insertion (Fig. 5g). This pattern of rescue in neuroinflammatory gene expression was not observed in the brain regions implanted with the SU-8 film (Supplementary Fig. 17b–d).

Discussion

In this study, we developed a transient shuttle for deep and widespread implantation of mesh electrodes without tangles. The main objective of transient shuttling via the PVA is to minimize secondary damage to brain tissue during insertion, withdrawal, and chronic implantation. A rigid and dissolvable PVA allows smooth penetration of brain tissue while decreasing

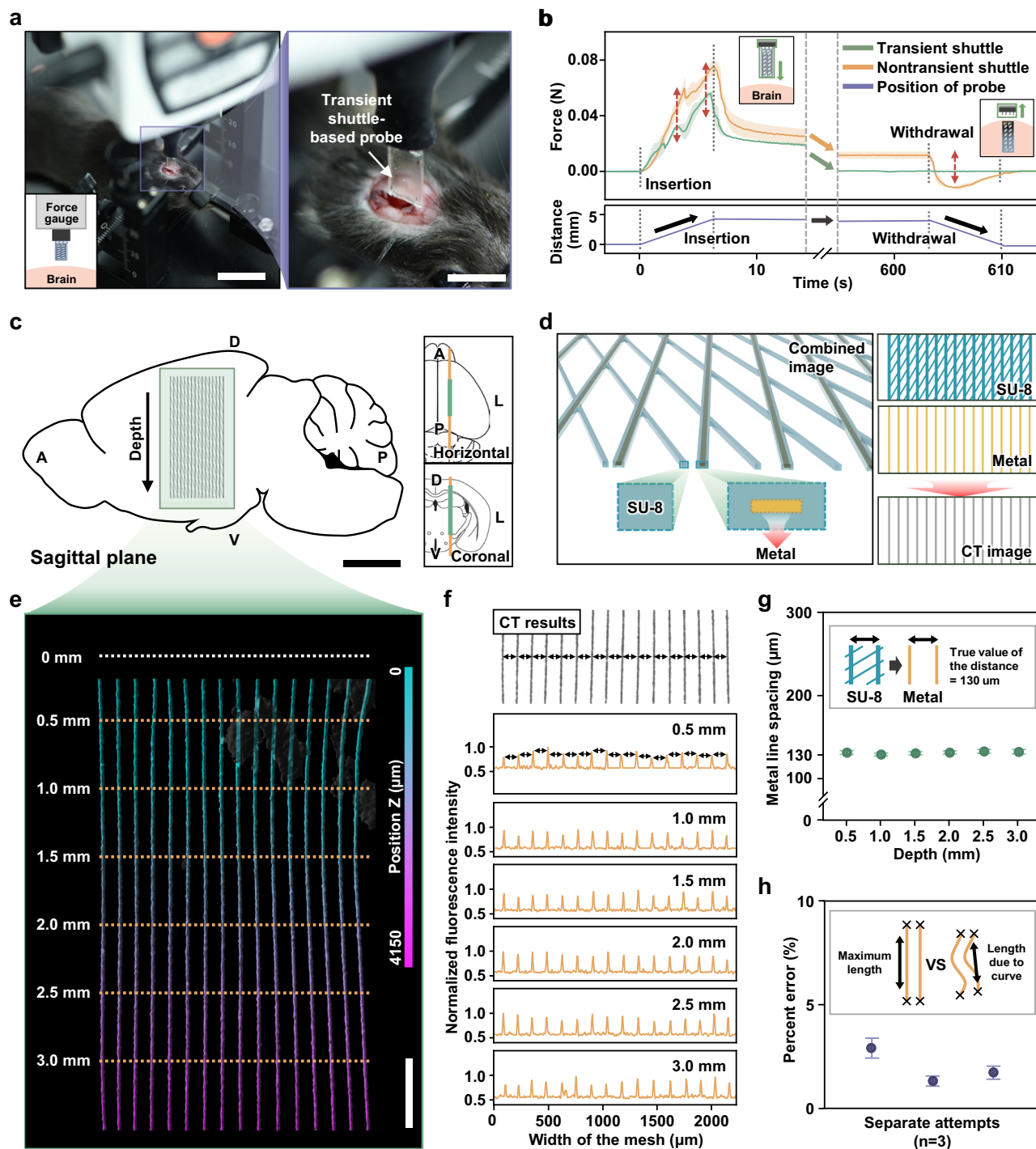


Fig. 4 | In vivo tests using mouse brain to explore the ability of the transient shuttle to implant the mesh electrode. a Photographs of the process of implantation of the transient shuttle-based probe (scale bar: 1 mm (left), 4 mm (right)). **b** Comparison of the force changes during insertion and withdrawal of the transient and non-transient shuttle-based probes into the mouse brain ($N = 3$; N is the number of the repeated measurements). **c, d** Schematic image of the layered structure of the

mesh electrode (scale bar: 2 mm). **e** Micro-CT image of the mesh electrode implanted in the mouse brain (scale bar: 500 μm). **f, g** Metal line spacing of the mesh electrode after its insertion into the mouse brain. **h** Bending degree of the metal line after insertion of the mesh electrode through the transient shuttle. All error bars reflect \pm s.e.m.

the footprint and friction between the probe and brain tissue. After insertion, the mesh electrode was separated by dissolving the PVA, preventing additional damage during the withdrawal of the inserter. Fully dissolved PVA also serves to reduce the stiffness of the mesh electrode (from rigid to flexible) while in the brain, such that the mesh electrode does not interrupt neuron regeneration or cause a severe immune response in the mouse brain. While our probe system has focused on the development of dissolvable

shuttles for the transport of mesh electrodes, the use of similar materials (e.g., biodegradable metal and polymer) for electrode and substrate can further reduce damage during extraction. The current design of the mesh probe and transient shuttle has a large dimension to emphasize the stable implantation of the transient shuttle without bending and buckling in a large area of the brain. Redesigning the dimension of the mesh probe and transient shuttle to fit the target area would reduce the damage to brain tissue.

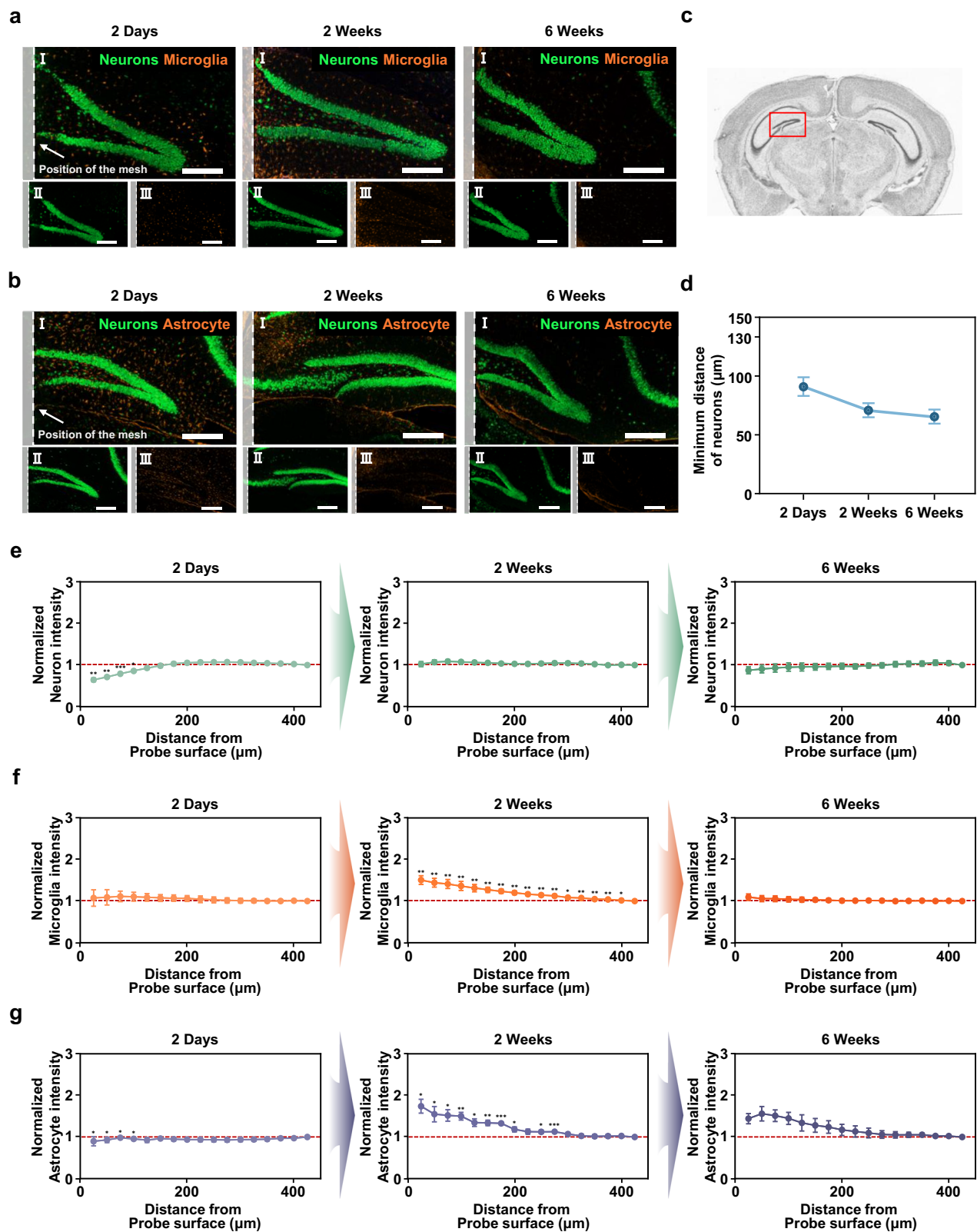


Fig. 5 | Histology studies of brain sections at 2 days, 2 weeks, and 6 weeks after implantation of the transient shuttle-based probe. **a** Microscopy images showing the neurons and microglia after implantation of the transient shuttle-based probe during each period (scale bar: 200 μm (top), 300 μm (bottom)). **b** Microscopy images showing the neurons and astrocytes after implantation of the transient shuttle-based probe during each period. **c** The brain regions shown in (a) and (b) (scale bar: 200 μm (top), 300 μm (bottom)). **d** Change in the distance between neurons and the implanted probe over time. **e** Fluorescence intensity of neurons at various distances from the probe. **f** Fluorescence intensity of microglia at various distances from the probe. **g** Fluorescence intensity of astrocytes at various distances from the probe. Time-dependent histology studies were repeated on $N = 3$ independent samples; all error bars represent \pm s.e.m.; * $P < 0.05$, ** $P < 0.01$, *** $P < 0.001$ (Student's t test).

200 μm (top), 300 μm (bottom)). **d** Change in the distance between neurons and the implanted probe over time. **e** Fluorescence intensity of neurons at various distances from the probe. **f** Fluorescence intensity of microglia at various distances from the probe. **g** Fluorescence intensity of astrocytes at various distances from the probe. Time-dependent histology studies were repeated on $N = 3$ independent samples; all error bars represent \pm s.e.m.; * $P < 0.05$, ** $P < 0.01$, *** $P < 0.001$ (Student's t test).

Additionally, reducing the thickness of the transient shuttle by applying a thinner PVA coating to the mesh electrode would enhance the minimization of damage during insertion. These alterations in design, involving reduced dimensions and thickness, will increase the possibility of bending and buckling in the transient shuttle due to decreased bending stiffness. Here, using slow-dissolvable materials with relatively high elastic modulus, including hyaluronic acid and poly(lactic-co-glycolic acid) (PLGA), can provide an opportunity to avoid bending of the shuttle. With these modifications, a fully dissolvable probe system could provide the opportunity for safe and wide brain mapping in a wide area.

Methods

Brain tissue phantom using agarose gel

The linear stage (ASM-1000; DigiTech, Osaka, Japan) was used to insert a brain probe into the agarose gel after the gel was inserted into the agarose gel. The agarose gel was polymerized by cooling after boiling in deionized water with gel-rose™ Agarose (AG113; Biofact, Daejeon, Republic of Korea). A digital force gauge (DFG35-0.12; Omega Engineering, Inc., CT, USA) was attached to the linear stage to measure the insertion and extraction forces. In the vibration experiment, a function generator (33210A, Keysight Technology, CA, USA) was used to input a sine signal of 17 Hz to a vibration amplifier (2100E21-100; The Modal Shop, OH, USA), which was connected to a vibration shaker (2007E; The Modal Shop, OH, USA) to vibrate the cantilever beam attached to a brain probe.

In vivo test using mice

Adult male mice (C57BL/6, 8–10 weeks old, 25–30 g, Jackson Laboratory) were housed under a 12-h light/dark cycle with free access to food and water. All procedures involving mice were approved by the Ajou University Institutional Animal Care and Use Committee. All the equipment was sterilized with 70% ethanol and under UV light for 12 hours before use. Mice were anesthetized via 5% isoflurane inhalation (Ifran; HANA Pharm Co., Seoul, Republic of Korea) and confirmed to be under anesthesia via tail pinch. The mice were then secured in a stereotaxic instrument (Kopf Model 940; David Kopf Instruments, Tujunga, CA) using a mouse anesthesia mask (Kopf mouse adapter model 907; David Kopf Instruments, Tujunga, CA). The anesthesia concentration was subsequently reduced to 1.5%. Eye ointment (Neodex Eye Oint; Hanlim Pharmaceutical Co., Seoul, Republic of Korea) was applied, and the scalp was wiped with an isopropyl alcohol 70% swab (FA Alcohol Swab; Firson Co., Gwangju, Republic of Korea) for sterilization before surgery. Approximately +1.5 mm of ML was removed from the midline to expose the skull. The probes, which were stored with desiccant, were cooled with liquid nitrogen and inserted through the hole in the skull made with a hand drill (Micromotor Strong 207 A; Saeshin Precision Co., Daegu, Republic of Korea) at a depth of 5 mm into the brain with rapid insertion. Presterilized PBS was used to gently flow between the probe body and the skull for approximately 10 min. Subsequently, the probe body was lifted vertically and removed. The scalp was sutured using sutures (#W502H Mersilk; Ethicon, Inc., NJ, USA), and antibiotic ointment (antibiotic ointment [Fucidin]; Dong-wha Pharmaceutical Co., Seoul, Republic of Korea) was applied around the wound.

Micro-CT imaging

Two days after probe insertion, the mice were transcardially perfused with PBS followed by 4% paraformaldehyde (PFA). Subsequently, the skull was carefully opened, and the brain was removed and placed in 4% PFA. After fixation, the brain was scanned using a Micro-CT (Xradia versa 620 imaging system, Zeiss, Dublin, CA) located at the Korea Basic Science Institute (Gwangju, Republic of Korea). The samples were scanned in custom-made sample holders that oriented the samples vertically on the stage and rotated them horizontally by 180° + fan. For whole-brain images, samples were taken 31 mm from the RA-Source and 87 mm from the RA-detector. The whole brain was scanned at 18 µm resolution using a 0.4× objective with an energy setting of 50 kV, 90 µA, and a power source of 4.5 W with an air filter

and 801 projections. For the brain, which included mesh electrode line images, samples were taken 42 mm from the RA-Source and 21 mm from the RA-detector and scanned at 4.5 µm resolution using a 4× objective with the following settings: 60 kV, 110 µA, 6.5 W, LE2 filter, and 1601 projections. Following scanning, all 2D and 3D images were reconstructed and visualized by VGStudio software and Dragonfly Pro software (Object Research Systems, QC, Canada).

Characterization of the transient shuttle-based probe

A glass wafer (4" Soda lime; AMGtech, Uiwang, Republic of Korea) was used as the fabrication substrate. Nickel was deposited as a sacrificial layer by sputtering (Q300T D Plus, Quorum Tech, East Sussex, UK) on a glass wafer. An SU-8 photoresist (2005, KAYAKU Advanced Materials, MA, USA) was used to construct the bottom and top layers of the three-layer structure. In the photolithography process, photoresists were coated using a spin-coater (SF-100NA; Rhabdos, Seoul, Korea) and then baked using a hot plate (SMHS-3; DAIHAN Scientific Co., Ltd., Wonju, Republic of Korea). We used a mask aligner (M150P, PROwin Co., Ltd., Daejeon, Republic of Korea) with an I-filter UV lamp to expose the mixture to a photoresist with a micropatterned chromium mask. The LOR (10C; KAYAKU Advanced Materials, MA, USA) and AZ5214-E (Merk KGaA, Darmstadt, Germany) photoresistors were used for the lift-off process to pattern a metal bilayer. The middle layer of the three-layer consisted of a metal bilayer of Ti/Au, which was deposited by a thermal evaporator (DDHT-SB015, Dae Dong High Tech, Co., Gimpo, Republic of Korea). A FeCl₃ anhydride (Samchun Chemicals, Seoul, Republic of Korea) was used to prepare a FeCl₃ solution. The FeCl₃ solution was employed to etch the Ni layer, enabling the achievement of mesh structures. A 3D printer (Projet MJP 2500; 3D Systems, SC, USA) was utilized to fabricate an inserter and a mold for a PDMS mold. We inserted 160 µm diameter acupuncture needles (Dongbang Medical, Boryeong, Republic of Korea) to help the transient shuttle adhere effectively to the inserter. We used a 9:1 mixture of PDMS (Sylgard™ 184; K1 Solution, Gwangmyeong, Republic of Korea) to fabricate the PDMS mold, which was subsequently used to align the inserter and the mesh structure at the proper position. PVA powder (#2000; Samchun Chemicals, Seoul, Republic of Korea) was used to make PVA solution, forming the transient shuttle.

Data availability

All the data needed to evaluate the conclusions in the paper are presented in the paper or in the Supplementary Materials.

Received: 17 February 2024; Accepted: 5 July 2024;

Published online: 13 July 2024

References

- Pizzo, F. et al. Deep brain activities can be detected with magnetoencephalography. *Nat. Commun.* **10**, 971 (2019).
- Lu, L. et al. Wireless optoelectronic photometers for monitoring neuronal dynamics in the deep brain. *Proc. Natl. Acad. Sci. USA* **115**, E1374–E1383 (2018).
- Rivnay, J., Wang, H., Fenno, L., Deisseroth, K. & Malliaras, G. G. Next-generation probes, particles, and proteins for neural interfacing. *Sci. Adv.* **3**, e1601649 (2017).
- Del Campo Fonseca, A. et al. Ultrasound trapping and navigation of microrobots in the mouse brain vasculature. *Nat. Commun.* **14**, 5889 (2023).
- Won, S. M., Cai, L., Gutruf, P. & Rogers, J. A. Wireless and battery-free technologies for neuroengineering. *Nat. Biomed. Eng.* **7**, 405–423 (2023).
- Fu, T.-M., Hong, G., Viveros, R. D., Zhou, T. & Lieber, C. M. Highly scalable multichannel mesh electronics for stable chronic brain electrophysiology. *Proc. Natl. Acad. Sci. USA* **114**, E10046–E10055 (2017).
- Chae, U. et al. A neural probe for concurrent real-time measurement of multiple neurochemicals with electrophysiology in multiple brain regions in vivo. *Proc. Natl. Acad. Sci. USA* **120**, e2219231120 (2023).

8. Shin, H. et al. Multifunctional multi-shank neural probe for investigating and modulating long-range neural circuits in vivo. *Nat. Commun.* **10**, 3777 (2019).
9. Taal, A. J. et al. Optogenetic stimulation probes with single-neuron resolution based on organic LEDs monolithically integrated on CMOS. *Nat. Electron.* **6**, 669–679 (2023).
10. Shin, H. et al. 3D high-density microelectrode array with optical stimulation and drug delivery for investigating neural circuit dynamics. *Nat. Commun.* **12**, 492 (2021).
11. Mohanty, A. et al. Reconfigurable nanophotonic silicon probes for sub-millisecond deep-brain optical stimulation. *Nat. Biomed. Eng.* **4**, 223–231 (2020).
12. Kim, K. et al. Artifact-free and high-temporal-resolution in vivo opto-electrophysiology with microLED optoelectrodes. *Nat. Commun.* **11**, 2063 (2020).
13. McGlynn, E. et al. The future of neuroscience: flexible and wireless implantable neural electronics. *Adv. Sci.* **8**, 2002693 (2021).
14. Salatino, J. W., Ludwig, K. A., Kozai, T. D. & Purcell, E. K. Glial responses to implanted electrodes in the brain. *Nat. Biomed. Eng.* **1**, 862–877 (2017).
15. Xie, C. et al. Three-dimensional macroporous nanoelectronic networks as minimally invasive brain probes. *Nat. Mater.* **14**, 1286–1292 (2015).
16. Kozai, T. D., Jaquins-Gerstl, A. S., Vazquez, A. L., Michael, A. C. & Cui, X. T. Brain tissue responses to neural implants impact signal sensitivity and intervention strategies. *ACS Chem. Neurosci.* **6**, 48–67 (2015).
17. Wellman, S. M. et al. A materials roadmap to functional neural interface design. *Adv. Funct. Mater.* **28**, 1701269 (2018).
18. Fu, T.-M. et al. Stable long-term chronic brain mapping at the single-neuron level. *Nat. Methods* **13**, 875–882 (2016).
19. Paulk, A. C. et al. Large-scale neural recordings with single neuron resolution using Neuropixels probes in human cortex. *Nat. Neurosci.* **25**, 252–263 (2022).
20. Lee, Y. et al. A lubricated nonimmunogenic neural probe for acute insertion trauma minimization and long-term signal recording. *Adv. Sci.* **8**, 2100231 (2021).
21. Zhang, S. et al. A removable insertion shuttle for ultraflexible neural probe implantation with stable chronic brain electrophysiological recording. *Adv. Mater. Interfaces* **7**, 1901775 (2020).
22. Zhou, T. et al. Syringe-injectable mesh electronics integrate seamlessly with minimal chronic immune response in the brain. *Proc. Natl. Acad. Sci. USA* **114**, 5894–5899 (2017).
23. Zhao, S. et al. Tracking neural activity from the same cells during the entire adult life of mice. *Nat. Neurosci.* **26**, 696–710 (2023).
24. Luan, L. et al. Ultraflexible nanoelectronic probes form reliable, glial scar-free neural integration. *Sci. Adv.* **3**, e1601966 (2017).
25. He, F., Lycke, R., Ganji, M., Xie, C. & Luan, L. Ultraflexible neural electrodes for long-lasting intracortical recording. *iScience* **23**, 101387 (2020).
26. Chu, J. P., Yu, C.-C., Tanatsugu, Y., Yasuzawa, M. & Shen, Y.-L. Non-stick syringe needles: beneficial effects of thin film metallic glass coating. *Sci. Rep.* **6**, 31847 (2016).
27. Cho, Y., Park, S., Lee, J. & Yu, K. J. Emerging materials and technologies with applications in flexible neural implants: a comprehensive review of current issues with neural devices. *Adv. Mater.* **33**, 2005786 (2021).
28. Deng, Z., Smolyanitsky, A., Li, Q., Feng, X.-Q. & Cannara, R. J. Adhesion-dependent negative friction coefficient on chemically modified graphite at the nanoscale. *Nat. Mater.* **11**, 1032–1037 (2012).
29. Guan, S. et al. Elastocapillary self-assembled neurotassels for stable neural activity recordings. *Sci. Adv.* **5**, eaav2842 (2019).
30. Pas, J. et al. A bilayered PVA/PLGA-bioresorbable shuttle to improve the implantation of flexible neural probes. *J. Neural Eng.* **15**, 065001 (2018).
31. Zhang, E. N. et al. Mechanically matched silicone brain implants reduce brain foreign body response. *Adv. Mater. Technol.* **6**, 2000909 (2021).
32. Jin, S. H. et al. Water-soluble thin film transistors and circuits based on amorphous indium–gallium–zinc oxide. *ACS Appl. Mater. Interfaces* **7**, 8268–8274 (2015).
33. Chen, P.-C., Young, C. G., Schaffer, C. B. & Lal, A. Ultrasonically actuated neural probes for reduced trauma and inflammation in mouse brain. *Microsyst. Nanoeng.* **8**, 117 (2022).
34. Chen, Z.-J. et al. A realistic brain tissue phantom for intraparenchymal infusion studies. *J. Neurosurg.* **101**, 314–322 (2004).
35. Shahab, S., Kasra, M. & Dolatshahi-Pirouz, A. Design and construction of a novel measurement device for mechanical characterization of hydrogels: a case study. *PLoS ONE* **16**, e0247727 (2021).
36. Zhou, Y. et al. A silk-based self-adaptive flexible opto-electro neural probe. *Microsyst. Nanoeng.* **8**, 118 (2022).
37. Li, J. et al. A tissue-like neurotransmitter sensor for the brain and gut. *Nature* **606**, 94–101 (2022).
38. Park, S. et al. Adaptive and multifunctional hydrogel hybrid probes for long-term sensing and modulation of neural activity. *Nat. Commun.* **12**, 3435 (2021).
39. Wang, Y., Yang, X., Zhang, X., Wang, Y. & Pei, W. Implantable intracortical microelectrodes: reviewing the present with a focus on the future. *Microsyst. Nanoeng.* **9**, 7 (2023).
40. Patil, A. C. & Thakor, N. V. Implantable neurotechnologies: a review of micro- and nanoelectrodes for neural recording. *Med. Biol. Eng. Comput.* **54**, 23–44 (2016).
41. Sharafkhani, N. et al. Neural tissue-microelectrode interaction: brain micromotion, electrical impedance, and flexible microelectrode insertion. *J. Neurosci. Methods* **365**, 109388 (2022).
42. Lind, G., Linsmeier, C. E. & Schouenborg, J. The density difference between tissue and neural probes is a key factor for glial scarring. *Sci. Rep.* **3**, 2942 (2013).
43. Wellman, S. M. & Kozai, T. D. Y. Understanding the inflammatory tissue reaction to brain implants to improve neurochemical sensing performance. *ACS Chem. Neurosci.* **8**, 2578–2582 (2017).

Acknowledgements

This work is supported by funding from the NRF of Korea (grant no. 2022R1C1C1005741, 2022R1A2C2093100, RS-2023-00217595, and RS-2023-00271830). We obtained new faculty research funding from Ajou University and funding from Ajou University. This work was supported by the Korea Environment Industry & Technology Institute (KEITI) through the Digital Infrastructure Building Project for Monitoring, Surveying, and Evaluating the Environmental Health Program, funded by the Korea Ministry of Environment (MOE) (2021003330009). We thank Prof. Huyk-Wan Ko at Yonsei University for generously providing the GFAP antibodies.

Author contributions

Y.R., H.K., E.K., and K.J. contributed equally to this work. Y.R. led the work. H.K. and K.J. designed and fabricated the transient shuttle-based probe. E.K. performed the in vivo experiments. M.K., S.I., I.H., J.P., S.J.P., Y.B., and J.-I.P. investigated and performed the experiments. G.D. performed the simulation modeling. S.H. and J.-S.K. contributed to the analysis of the mechanical characterizations of the probe. E.J.L. and D.K. supervised the work.

Competing interests

The authors declare no competing interests.

Additional information

Supplementary information The online version contains supplementary material available at <https://doi.org/10.1038/s41528-024-00328-w>.

Correspondence and requests for materials should be addressed to Eun Jeong Lee or Daeshik Kang.

Reprints and permissions information is available at <http://www.nature.com/reprints>

Publisher's note Springer Nature remains neutral with regard to jurisdictional claims in published maps and institutional affiliations.

Open Access This article is licensed under a Creative Commons Attribution 4.0 International License, which permits use, sharing, adaptation, distribution and reproduction in any medium or format, as long as you give appropriate credit to the original author(s) and the source, provide a link to the Creative Commons licence, and indicate if changes were made. The images or other third party material in this article are included in the article's Creative Commons licence, unless indicated otherwise in a credit line to the material. If material is not included in the article's Creative Commons licence and your intended use is not permitted by statutory regulation or exceeds the permitted use, you will need to obtain permission directly from the copyright holder. To view a copy of this licence, visit <http://creativecommons.org/licenses/by/4.0/>.

© The Author(s) 2024